

FastSPECT II: System Characterization and Small-Animal Imaging

Journal:	<i>IEEE Transactions on Nuclear Science</i>
Manuscript ID:	TNS-00553-2013
Manuscript Type:	Imaging and Instrumentation for Nuclear Medicine
Date Submitted by the Author:	26-Aug-2013
Complete List of Authors:	Chen, Yi-Chun; National Central University, Dept. Optics and Photonics Furenli, Lars; University of Arizona, Medical Imaging and Optical Sciences Liu, Zhonglin; University of Arizona, Dept. Medical Imaging Barrett, Harrison; University of Arizona, Medical Imaging and Optical Sciences
Standard Key Words:	SPECT instrumentation, Calibration, Imaging

FastSPECT II: System Characterization and Small-Animal Imaging

Yi-Chun Chen, Lars R. Furenlid, *Member, IEEE*, Zhonglin Liu, and Harrison H. Barrett, *Fellow, IEEE*

Abstract—FastSPECT II is a stationary small-animal SPECT imager built with 16 modular scintillation cameras and listmode data-acquisition electronics. The instrument is equipped with exchangeable aperture assemblies and adjustable camera positions for selections of magnifications, pinhole sizes, and fields of view (FOVs). The measurement of the imaging system matrix (1 mm³ voxels) and the positioning of imaging subjects are supported by a five-axis motion-control system. The calibration data of individual cameras are utilized to construct the statistical model of the maximum-likelihood position estimator. A system matrix with voxels on 0.5 mm grid is generated by the centroid interpolation with Gaussian fitting method.

Spatial resolution of the system is evaluated by the Fourier crosstalk approach and visualized through a miniature hot-rod phantom. Imaging of the mouse bone and kidneys illustrates the ability of FastSPECT II to provide high-quality small-animal images. The dynamic imaging capability of the imager is validated via mouse tumor studies. Mouse femur images demonstrate the sub-millimeter resolution of FastSPECT II in the high magnification (18×) configuration.

Index Terms—Dynamic, listmode, small animal, SPECT, stationary

I. INTRODUCTION

THE purpose of SPECT imaging is to recover the radiotracer distribution in the object from the measured image data. To accomplish SPECT imaging, sufficient projections from different views must be collected to allow tomographic reconstruction. This can be done by rotating the object in front of the detector or by rotating the collimator-detector combination around the object. Another approach is to adopt the stationary SPECT design, in which adequate angular views are recorded simultaneously without any motion of the cameras or the imaging subject [1]-[6]. Stationary SPECT usually incorporates multiple cameras in a closed ring or polygon, or in multiple rings to acquire sufficient angular sampling. More

detectors lead to higher system sensitivity but also higher cost.

To achieve a favorable compromise among the spatial resolution, sensitivity, and field-of-view (FOV), pinhole collimations are usually utilized in preclinical SPECT systems. Current stationary SPECT systems can be roughly classified into two categories: one uses high resolution cameras in small modules and single pinhole per camera [2], [4], [6], and the other uses cameras with a large area and multiple pinholes per camera [3], [5]. In either case, sufficient angular sampling has to be recorded for tomographic reconstruction. The stationarity enables dynamic imaging capability of the imager.

FastSPECT (Four-dimensional Arizona STationary Single-Photon Emission Computed Tomography) is the name of a SPECT imaging architecture developed at the University of Arizona in the 1980s. The Center for Gamma-Ray Imaging (CGRI) at the University of Arizona has developed three stationary small-animal SPECT systems in the past two decades, including FastSPECT [7], FastSPECT II [2], and FastSPECT III [6], [8].

FastSPECT was originally developed for dynamic 3D human-brain imaging [1] and has been transformed to a small-animal imager by incorporating a high-resolution pinhole aperture [9]. The system consists of 24 modular scintillation cameras, each containing a 5mm-thick NaI(Tl) scintillation crystal coupled to 2 × 2 PMTs and having its own front-end electronics [10]-[12]. FastSPECT II is a second generation of the FastSPECT system featuring redesigned modular scintillation cameras and listmode data-acquisition electronics, and equipped with more flexible system gantry and enclosure, exchangeable aperture assemblies, and an improved calibration and positioning system. A more detailed introduction to FastSPECT II is presented in section II.

FastSPECT III [6], [8] is the third generation of the FastSPECT concept. It is dedicated to rodent neurological studies and utilizes high-resolution CCD-based gamma cameras called BazookaSPECT. Each BazookaSPECT camera is composed of a columnar CsI(Tl) scintillator, an image intensifier, an optical lens set, and a CCD with 640 × 480 pixels and up to 200 frames per second. FastSPECT III has 20 BazookaSPECT detectors arranged in three rings: a central ring of ten and two outer rings of five focusing at a common spherical FOV of about 15 mm. Custom imaging apertures and pinhole inserts are fabricated by 3D printing and casting technology. Image data are transferred to 5 processing computers with a total of 20 CPU cores and 20 GPUs. The system is capable of processing more than 10⁹ pixels per second

Manuscript received August 26, 2013. This work was supported in part by the National Institutes of Health under Grant P41 EB002035 and National Science Council under Grant NSC-101-2918-I-008-010.

Y. C. Chen is with the Department of Optics and Photonics, National Central University, Taiwan (e-mail: ycchen@dop.ncu.edu.tw).

L. R. Furenlid and H. H. Barrett are with the Center for Gamma-ray Imaging and the Department of Medical Imaging, University of Arizona, Tucson, AZ 85724, USA. They are also with the College of Optical Sciences, University of Arizona, Tucson, AZ 85721, USA (e-mail: furen@radiology.arizona.edu; barrett@radiology.arizona.edu).

Z. Liu is with the Center for Gamma-ray Imaging and the Department of Medical Imaging, University of Arizona, Tucson, AZ 85724, USA (e-mail: zliu@radiology.arizona.edu).

and the 20 cameras provide a space-bandwidth product of about 2×10^6 .

This paper describes FastSPECT II and its capabilities. Section II describes the hardware components and the instrument control kernel. Section III presents the system characterization and performance evaluation. Small-animal imaging with FastSPECT II is presented in section IV to demonstrate the dynamic imaging capability and sub-millimeter resolution of the system. Section V discusses potential future developments and applications of FastSPECT II. A summary of this study is given in section VI.

II. FASTSPECT II

FastSPECT II is a stationary small-animal SPECT imager built with modular scintillation cameras and listmode data-acquisition electronics [2]. Fig. 1 shows photographs of FastSPECT II. The instrument is housed in a lead-shielded enclosure and has exchangeable aperture assemblies and adjustable camera positions for selection of the magnifications, pinhole sizes, and fields of view (FOVs).

A. Hardware Components

The modular scintillation camera in FastSPECT II comprises a 5mm-thick NaI(Tl) scintillation crystal (4.5-inch \times 4.5-inch area), a 15mm-thick fused quartz light guide, and a 3×3 array of 1.5-inch diameter head-on PMTs. A single high-voltage (HV) connector drives all nine PMTs in parallel, with extra decoupling capacitors installed across the individual voltage-divider networks. Each PMT has 10 dynode stages and operates at around -800V. Individual SMB connectors bring out the signals from the PMT anodes for connection to the transimpedance amplifiers of the acquisition electronics. The cameras were manufactured to our specifications by Teledyne Brown Engineering of Huntsville, AL.

As shown in Fig. 1(a), FastSPECT II is built in and around a welded tubular aluminum framework. Sixteen cameras are arranged in two octagonal rings on opposite side of a pair of central plates. One ring is rotated by 22.5 degrees with respect to the other. A central lead baffle can be inserted between the central plates to prevent image multiplexing. Each camera has an aluminum mounting plate to be captured in a milled recess. Three radial camera positions of different distance (16.51, 24.13, and 31.75 cm) from the imager axis can be selected. The surface normal of each camera is perpendicular to the imager axis. The front-end electronics associated with each camera is mounted in proximity to the camera it serves.

The entire imager is shielded with 3.18 mm lead sheet laminated to a 3.18-mm-thick powder-coated aluminum skin. Two hinged doors, one on each side, provide the access to service the interior components or to change the camera positions. All cables run through a cable maze on the roof of the housing; the cables include HV BNC-connector coaxial cables that provide the camera high voltage, power cords that supply the front-end event-processor boards, and Ethernet cables that link up the front-end with the back-end electronics. The entire structure is built on a heavy-duty wheeled base that permits relocation of the imager if necessary.

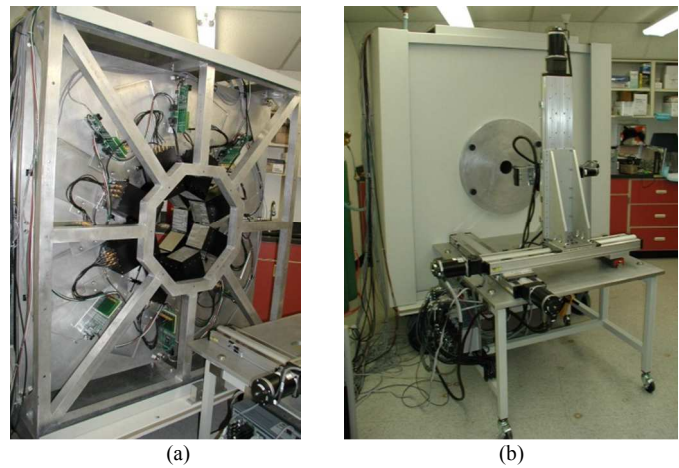


Fig. 1 Photographs of FastSPECT II: (a) the framework, modular cameras and front-end electronics; (b) the enclosed imager and the positioning system.

The imaging geometry of FastSPECT II can be adjusted to accommodate imaging studies with different resolution requirements. Aperture cylinders with different diameters can be used in combination with radial camera positions to achieve a variety of imaging magnifications and fields of view. Pinhole diameters can also be changed accordingly to match the desired spatial resolution, with the intrinsic resolution of the modular cameras taken into account. The achievable magnification ranges from 2.4 to 18, the pinhole diameter varies from 0.1 to 1.0 mm, and the FOV covers from 5 to 40 mm in three directions.

In its low-magnification (2.4 \times) configuration, FastSPECT II employs an array of 1-mm-diameter pinholes, one per camera, as the image-forming element. The pinholes are precisely-machined gold disks mounted in the milled recesses of a lead cylinder. The 0.79-cm-thick lead pipe has 10.74 cm outer diameter and the gold pinholes are 4.83 cm from the imager axis. The gold inserts are held in place with retaining rings and can be conveniently exchanged for other inserts with alternative pinhole diameters. The pinholes are arranged so that a point source located at the center of the FOV will be projected to the center of each camera. All cameras look at the FOV from an oblique angle. With the closest camera position (6.5 inches from the imager axis) and this aperture cylinder, FastSPECT II provides a magnification of approximately 2.4. The FOV is about 40 mm in three directions, which accommodates a typical laboratory mouse (25-50 grams).

A five-motion positioning system is implemented as shown in Fig. 1(b). The motion system comprises a 6K6 motion controller, four linear stages, and one rotary stage, all from Parker Hannifin Corporation. The 6K6 motion controller can accommodate up to six stepper/servo motors and move multiple stages at the same time. It communicates with the host computer via a crossover Ethernet 10Base-T cable. Three linear stages implement the standard x-y-z motions. The base stage has 700-mm travel while the other two have 600-mm travel. An electromagnetic brake is applied to the vertical stage to prevent backdriving due to gravity. A rotary stage and a small secondary translation stage with 150-mm travel are mounted on the vertical stage. This combination makes it possible to

measure the mean detector response function (MDRF) scans of individual cameras with the convenience of having two translation axes parallel to any camera face.

Each of the four linear stages is equipped with hardware limit switches at two ends of travel and a home switch in the middle. Additional software limit switches can be added if necessary. The rotary stage has a magnetic home switch and can rotate over 360 degrees with no limitation. However, it is protected by software limit switches from wrapping the wiring around. Microstepping motors along with optical encoders enable all stages running in servo control and provide repeatable positioning with 1.25 μm linear precision and 1 millidegree rotary precision.

B. Electronics and Data Architecture

FastSPECT II adopts raw listmode acquisition architecture. The full set of observations associated with a gamma-ray event is recorded as an entry in an ordered list. Attributes of each individual event include an identifier for the camera where the event is detected, the nine signal values present in the 3×3 array of PMTs, and the time of occurrence. Listmode data collection offers several advantages over traditional binned-mode acquisition, such as efficient data storage when there are more than four attributes, full information preservation, direct dynamic-imaging capability, and more data-processing flexibility [13]-[17].

The data-acquisition task in FastSPECT II is divided into two parts, a front-end that performs digital event detection and listmode entry generation, and a back-end that buffers data and communicates with the host computer [18], [19]. One listmode event-buffer board supports two cameras, so there are sixteen front-end event processors and eight back-end event-buffer boards in FastSPECT II.

The operation of the listmode data-acquisition system is diagrammed in Fig. 2. Camera events are detected with a fully-pipelined event-detection algorithm. Signals from PMT anodes are shaped with analog filters and digitized to 12 bits with free-running analog-to-digital converters (ADCs). A continuous stream of nine 12-bit data words every 30 nanoseconds are summed and scanned for an event maximum by a combination of threshold trigger and first-derivative zero-crossing detection. A pile-up rejector is implemented to hold a detected event long enough so that no second trigger can occur within the support of the analog shaping amplifiers. Each event detection is completed in six stages driven by a 33-MHz clock. 3.5 gigabits of raw data per second are digested in each processor. Event attributes are assembled into data packets and transmitted to back-end buffers via a network-based SERDES (serializer/deserializer) chipset with auto-synchronization. Data arrays are transformed into a low-voltage differential-signaling (LVDS) serial data stream by the serializer on the front-end board, sent across to the deserializer on the back-end board via a standard category-5 twisted-pair cable, retained in the event buffers, and eventually saved in the host computer through a PCI interface.

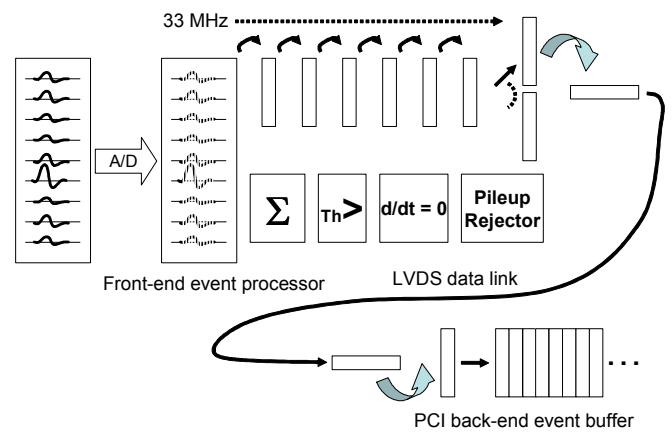


Fig. 2 Block diagram representation of the operation of the listmode data acquisition system.

Gamma-ray events detected by FastSPECT II are saved in sixteen separate files, one for each camera. All observations associated with a gamma-ray event are recorded with their full acquired precision. The data comprise the peak amplitudes of the shaped PMT signals and the time of occurrence. The PMT signals are digitized to 12 bits with 1 sign bit and 11 data bits, and hence range from -2048 to 2047 in AD units. Nevertheless, only non-negative values are valid for true gamma-ray events. The time stamps are in 30-ns clock ticks counting from 0 to 4,294,967,295, which cycles about every 2 minutes. The camera ID is implicitly part of the event-list entry, although it is stored in the file name rather than inside the file with the PMT values and time stamps.

C. Instrument Control Kernel

FastSPECT II is controlled by two PCs running Windows[®] XP operating systems. Four listmode event-buffer boards are located in each of the PCs to support the full complement of 16 cameras. A custom device driver and low-level dynamic link libraries (DLLs) are responsible for recognizing the presence of listmode event-buffer boards on the PCI buses and providing memory-mapped I/O functions. A small Beowulf cluster consisting of four dual-CPU nodes is implemented to perform rapid position estimation for real-time planar-projection display. High-level instrument control is accomplished via custom GUI software programmed in the LabVIEW[™] environment. Both control PCs can run the imager control software independently, or they can execute the same control software simultaneously with one being the master and the other being a slave. Coordination between the two PCs and control of the robotic system are accomplished via TCP/IP communications. PVM (Parallel Virtual Machine) software is utilized to integrate the UNIX nodes and Windows machines into a single large parallel computer.

III. SYSTEM CHARACTERIZATION

A. Individual Camera Calibration: Measurement of the Mean Detector Response Function (MDRF)

The calibration of individual scintillation camera starts from the gain adjustment of each PMT followed by the measurement of the mean detector response function (MDRF) with a

collimated ^{99m}Tc source. This calibration is performed with the cameras mounted in the imager but no pinholes or collimator in place.

A Cerrobend-cast tube carrying a radioactivity-filled syringe cap provides a collimated beam of gamma rays with a beam size of 0.84 mm at zero distance and a beam divergence of 0.056 radians. The source count rate is designed to be more than 30 times that of the environmental radiation. When the modular camera is mounted in the imager with the shielding of the system enclosure but not the aperture cylinder, the background count rate is 70 cps on average. The efficiency of the Cerrobend collimator is 273 cps/mCi. The radioactive beam is oriented normal to the camera face during the calibration procedure with a distance of approximately 1 mm.

The nine PMTs of each FastSPECT II modular camera are operated with a single high voltage setting at around -800V. Even so, the electron gain of each PMT still differs due to fabrication variations. As described in section II-B, the analog PMT output is digitized to 12-bit words (1 sign bit and 11 data bits) with a free-running ADC on the front-end board. In order to utilize the full dynamic range of the ADCs, a collimated ^{99m}Tc source is scanned across the camera face to the center of each PMT and the reference voltage of the ADC is adjusted based on the PMT pulse-height spectrum. Fig. 3 shows a typical pulse-height spectrum of a single PMT output with 36,000 gamma-ray events acquired. All ADCs have a reference voltage of 2 volts at the beginning of the calibration procedure. When the collimated source is centered on one PMT, the control software alters the reference voltage of the ADC associated with that PMT so that the photopeak is roughly at 1,500 analog-to-digital units (ADU). This process is repeated for all nine PMTs to complete the gain adjustment.

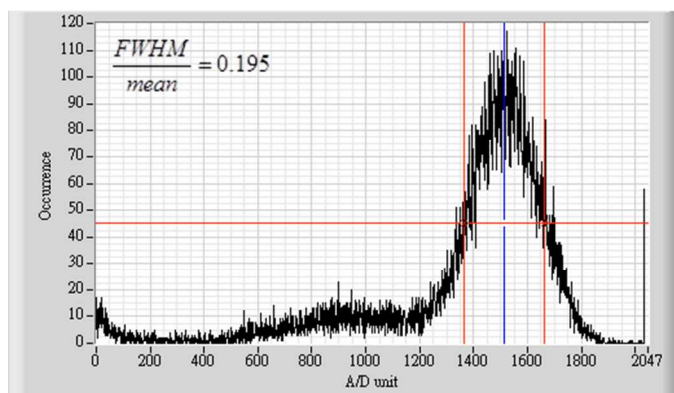


Fig. 3 Typical pulse-height spectrum of a single PMT output of a modular camera with a collimated ^{99m}Tc source centered on the PMT. The bin size used for plotting the histogram is 1 ADU.

To characterize the detector response, a collimated ^{99m}Tc source is scanned in a 2D grid pattern across the camera face. Thousands of gamma-ray events are collected at each calibration grid point. This measurement yields samples from the mean detector response function (MDRF) of the scintillation camera, defined as the average signal output of each PMT in the camera as a function of the gamma-ray incident position upon the camera face. A measured MDRF incorporates all optical and electronic properties of the

scintillation camera. Fig. 4 shows an *in situ* MDRF acquisition of a modular camera in the FastSPECT II system. The scan contains 78×78 points and the grid spacing is 1.5 mm to cover the 115-mm crystal width. More than 5,000 scintillation events are collected at each position and the total acquisition time is about 3.5 hours per camera.



Fig. 4 *In situ* MDRF acquisition of a modular camera in FastSPECT II.

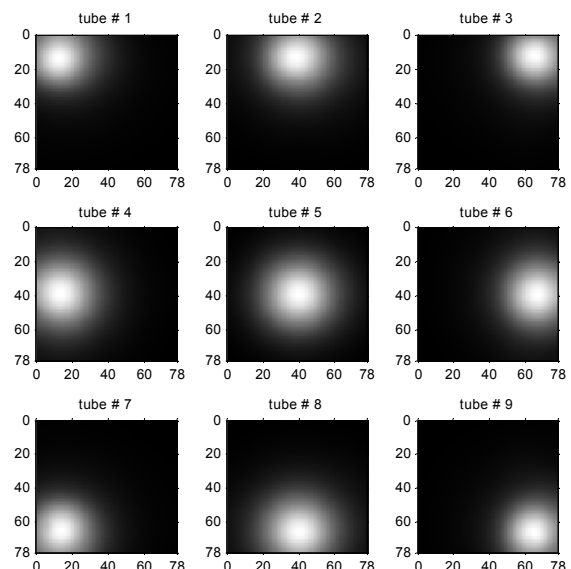


Fig. 5 The mean response of all nine PMTs as a function of the collimated source location.

The MDRF calibration data set is used to calculate the sample means and variances of the PMT signals as a function of the collimated source location. The sample means and variances are calculated for the events in the photopeak in several steps. First, histograms of the PMT signals are plotted, including one histogram for the sum signals of the nine PMTs and nine histograms for individual PMTs. Second, events outside the photopeak are removed by a multi-step algorithm to eliminate the noise tail and scattered events. Third, sample means and variances of the filtered data are calculated. Finally, the MDRF is smoothed by an adaptive least-squares polynomial fit to eliminate the Poisson measurement noise in the MDRF calibration [20], [21]. Fig. 5 shows the MDRF (the mean response as a function of the collimated source location of all nine PMTs) of one modular camera.

B. Measurement and Interpolation of the System Matrix

Linear digital-imaging systems are most accurately described as mappings from an object, which is a function of continuous variables, to a discrete set of measurements [22]. For numerical computations, the object is usually approximated by a linear combination of some expansion functions. One common choice is to discretize the 3D object $f(\mathbf{r})$ using voxel functions as

$$f_a(\mathbf{r}) = \sum_{\mathbf{n}=1}^N \theta_{\mathbf{n}} \phi_{\mathbf{n}}(\mathbf{r}), \quad (1)$$

where subscript a denotes approximate, \mathbf{n} is a 3D index to indicate the location in the object space, $\phi_{\mathbf{n}}(\mathbf{r})$ is a voxel function, which is uniform within a cube centered on point $\mathbf{r}_{\mathbf{n}}$, and $\theta_{\mathbf{n}}$ are the expansion coefficients. Hence the image-forming mechanism of a linear digital-imaging system can be formulated as a matrix mapping,

$$\mathbf{g} = \mathbf{H}\boldsymbol{\theta} + \boldsymbol{\varepsilon}, \quad (2)$$

where \mathbf{H} represents the system matrix and $\boldsymbol{\varepsilon}$ contains the modeling error due to discretization plus the measurement noise. Imaging systems are designed to recover the object function from the measured image vector. Image reconstruction is essentially an inverse problem to solve (2) for the object expansion coefficients $\boldsymbol{\theta}$ and requires accurate knowledge of the system matrix \mathbf{H} . The elements of \mathbf{H} can be expressed as

$$H_{\mathbf{mn}} = \int d^3r h_{\mathbf{m}}(\mathbf{r}) \phi_{\mathbf{n}}(\mathbf{r}), \quad (3)$$

where \mathbf{m} is a 3D multi-index to specify the projection angle and the 2D location on the detector face, and $h_{\mathbf{m}}(\mathbf{r})$ represents the system sensitivity function. Equation (3) shows that a column of \mathbf{H} matrix is the image of $\phi_{\mathbf{n}}(\mathbf{r})$ for all projection angles. Furthermore, when properly normalized, $H_{\mathbf{mn}}$ can be viewed as the probability that a photon emitted from voxel \mathbf{n} is detected in detector bin \mathbf{m} .

The system matrix of an imaging system can be obtained by many methods, such as analytic calculation, simulation, empirical determination, or some combination of these methods. The analytic or simulation method generates the \mathbf{H} matrix by making certain assumptions about the geometry and response of the system, and the empirical method measures the \mathbf{H} matrix directly. The simulation and measurement of the \mathbf{H} matrices of emission tomographic systems can be traced back to 1970's. Tipton [23] simulated the point response function for each point in the object space of his tomographic system, stored the whole system matrix on magnetic tapes, and used this matrix in his background subtraction algorithm for image reconstruction. Lefkoupoulos *et al.* [24] measured the \mathbf{H} matrices experimentally for their 2D and 3D tomographic systems. The maximum number of measured voxels was 144 in their study. They used the generalized inverse of the \mathbf{H} matrix as calculated by singular-value decompositions (SVD) for image reconstruction. As a measured \mathbf{H} matrix automatically takes account of the detector blur and non-uniformity, imager

geometry, radiometry, pinhole penetration, aperture defects, and system misalignment, we have preferred to carefully calibrate the imaging system and used the calibration data set as the \mathbf{H} matrix.

The \mathbf{H} matrix is measured by stepping a small, pointlike source of ^{99m}Tc through a 3D grid in the field of view (FOV) of the imager. The recipe suggested by Dr. A. B. Brill for making the point source is as follows: Chromatographic resin beads 300 μm in diameter are soaked in an aqueous solution of sodium pertechnetate and heated to dry. The beads are then glued together in an epoxy ball at the tip of a carbon-fiber tube to make a point source with about 1-mm diameter and more than 370-MBq radioactivity.

A typical calibration data set for FastSPECT II contains about 50,000 calibration points with 1-mm grid spacing to cover a cylindrical FOV of 41-mm length and 41-mm diameter. The acquisition time for the first grid point is set to acquire more than 1,000 events per camera, and the acquisition time for subsequent grid points is elongated according to the radioactive decay. The average sensitivity of FastSPECT II over the FOV is 243 cps/MBq. The total acquisition time for the \mathbf{H} -matrix calibration is about 24 hours, 4 half-lives of ^{99m}Tc . This measurement calibrates the imaging properties of the system, such as pinhole sizes and locations, camera orientations, and system sensitivity. Fig. 6 shows one column of the \mathbf{H} matrix, the images of the point source for all 16 projection angles.

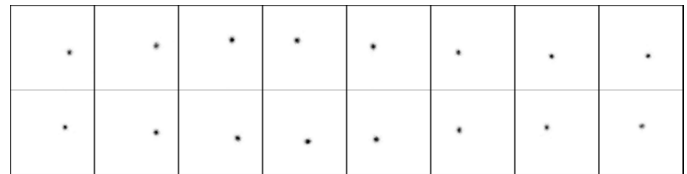


Fig. 6 One column of \mathbf{H} , the images of the point source for all 16 projection directions, when the source is located at voxel (20, 20, 30).

The spacing between calibration grid points defines the voxel size, and this spacing acts as the ultimate limit on the system resolution. A two-fold reduction in the voxel spacing increases the matrix size by a factor of 8. At the same time, the measurement time will be magnified by more than eightfold considering the radioactive decay. If we want to shrink the voxel spacing to achieve finer grids in image reconstruction, the calibration procedure will become increasingly burdensome.

One way for reducing this burden is to interpolate between calibration points. The idea of \mathbf{H} -matrix interpolation was first discussed and proved to be viable by Roney [25] in his thyroid phantom study. Later on, Rowe [26] simulated and measured the \mathbf{H} matrix of a pinhole SPECT system, decomposed it into two matrices, and interpolated the \mathbf{H} matrix based on the centroid locations and magnitudes of the pinhole projections. He also briefly discussed the possibility of fitting a Gaussian function to the detector projection data. In order to reduce the system-calibration time and achieve finer reconstruction grids, two schemes for interpolating \mathbf{H} have been proposed in our previous study [27]: these are centroid interpolation with Gaussian fitting and Fourier interpolation method. In this paper,

the centroid interpolation with Gaussian fitting method is utilized to interpolate the \mathbf{H} matrix.

The point response of a pinhole SPECT system is approximately shift-invariant for lateral translations of the point source with respect to the detector face and slowly varying for longitudinal translations [22]. As shown in (3) and Fig. 6, one column of \mathbf{H} is the image of the voxel function $\phi_n(\mathbf{r})$ for all projection angles. Fig. 6 also reveals that the projection of the point source looks like a blob on the detector face. Therefore, each column of \mathbf{H} can be parameterized into its centroid on the detector and a spread about the centroid as

$$H_{mn} = h_{jn} [\mathbf{m} - \mathbf{m}_c(\mathbf{n}, j)], \quad (4)$$

where $\mathbf{m}_c(\mathbf{n}, j)$ denotes the centroid of the image of $\phi_n(\mathbf{r})$ on the detector for the j^{th} projection angle, and $h_{jn} [\mathbf{m} - \mathbf{m}_c(\mathbf{n}, j)]$ is a blur function around the centroid. Since columns of \mathbf{H} are slowly varying for adjacent point source locations, it is possible to interpolate the \mathbf{H} matrix by averaging the centroid locations and the blur functions $h_{jn}(\mathbf{m})$ for neighboring point source locations.

The blur functions $h_{jn}(\mathbf{m})$ can be approximated to the first order by considering the point source as a uniform sphere, calculating its geometric projection through a circular pinhole and convolving with the detector point spread function [28]. In practice, the blur functions suffer from pinhole penetration [29] and contain photon-counting noise in measurements. A simple 2D Gaussian model is used to parameterize the blur functions $h_{jn}(\mathbf{m})$ in this research work. More sophisticated models can be adopted to mimic the blur functions for different imager geometry and detector physics.

For each measured point-source projection, a 2D Gaussian that best fits the image in least-square sense is estimated by the Levenberg-Marquardt method adopted from [30]. The blur function on a single camera can be expressed as

$$h_{jn}(x, y) = \frac{A}{2\pi\sqrt{\det \mathbf{K}}} \exp \left\{ -\frac{1}{2} \begin{bmatrix} x - \bar{x} & y - \bar{y} \end{bmatrix} \mathbf{K}^{-1} \begin{bmatrix} x - \bar{x} \\ y - \bar{y} \end{bmatrix} \right\}, \quad (5)$$

and the covariance matrix can be decomposed into its eigenvalues and the rotation angle of the principal axis as

$$\mathbf{K} = \mathbf{R}_\phi \mathbf{K}_0 \mathbf{R}_\phi^t = \begin{bmatrix} \cos \phi & \sin \phi \\ -\sin \phi & \cos \phi \end{bmatrix} \begin{bmatrix} \lambda_1 & 0 \\ 0 & \lambda_2 \end{bmatrix} \begin{bmatrix} \cos \phi & -\sin \phi \\ \sin \phi & \cos \phi \end{bmatrix}. \quad (6)$$

Therefore each blur function is parameterized into six coefficients, including the amplitude A , the centroid location (\bar{x}, \bar{y}) , and the eigenvalues λ_1 and λ_2 and the principal angle ϕ of the covariance matrix. The response between adjacent point-source locations are interpolated by averaging the Gaussian coefficients. Arithmetic averaging is applied to the amplitudes, centroid locations, and principal angles of the covariance matrices while geometric averaging is applied to the eigenvalues of the covariance matrices to approximate the magnification effect. The \mathbf{H} matrix is then regenerated from the

interpolated Gaussian coefficients. Pixels that are away from the centroid location with a distance more than three standard deviations are assigned zero values and not saved in the interpolated \mathbf{H} matrix. In addition, the blur functions correspond to the original measured voxels are also replaced by their Gaussian fits in an interpolated \mathbf{H} matrix.

C. Maximum-Likelihood Position Estimation and Likelihood Windowing

When a scintillation event is detected in a modular camera, the interaction location can be estimated by using the strength of PMT outputs and a proper position estimator. A maximum-likelihood (ML) position estimator [12] is constructed using a scaled Poisson model [31] and the MDRF of each camera.

Assume $\bar{V}_i(x, y)$ is the mean voltage output of the i^{th} PMT calculated from the MDRF calibration data set when the collimated source is located at position (x, y) . The gain G_i of each PMT is estimated by

$$G_i = \text{Var} \{V_i\} / \bar{V}_i, \quad (7)$$

with more than 30,000 events acquired when the collimated source is located at the center of the particular PMT in interest. Therefore for each scintillation event, the PMT responses V_i can be converted back into units of photoelectrons as

$$U_i = \text{round} \left(\frac{V_i}{G_i} \right). \quad (8)$$

If we consider a monoenergetic source and assume that the camera response is insensitive to the depth of interaction (DOI), the scaled Poisson model for each lateral coordinate (x, y) on the camera face is

$$\text{Pr}(\mathbf{n} | x, y) = \prod_{i=1}^9 \exp(-\bar{n}_i) \frac{\bar{n}_i^{n_i}}{n_i!}, \quad (9)$$

where the mean number of photoelectrons $\bar{n}_i(x, y)$ is

$$\bar{n}_i(x, y) = \text{round} \left(\frac{\bar{V}_i(x, y)}{G_i} \right). \quad (10)$$

For each detected scintillation event, a set of PMT responses $\{V_i\}$ is recorded and converted to $\{U_i\}$ in units of photoelectrons. The ML estimate for the interaction location is therefore

$$(\hat{x}_{ML}, \hat{y}_{ML}) = \arg \max_{x, y} [\ln \text{Pr}(\mathbf{U} | x, y)]. \quad (11)$$

More details on the maximum-likelihood position estimation can be found in [32].

Once the ML estimate of the scintillation position is obtained, a subsequent scatter-rejection technique is usually applied to discriminate against scattered events [33], [34]. In this study, each event is classified as scattered or unscattered by a position-dependent likelihood window. An event is accepted if

the resulting maximized likelihood satisfies the following criterion,

$$Pr(\mathbf{U} | \hat{x}_{ML}, \hat{y}_{ML}) > L_0(\hat{x}_{ML}, \hat{y}_{ML}), \quad (12)$$

where $L_0(x, y)$ is a position-dependent threshold computed from the MDRF calibration data. All events acquired in the MDRF calibration are processed to find their ML position estimates and corresponding log-likelihood values. An outlier filter calculates the sample mean and variance of the log-likelihood values, iteratively discards events outside two standard deviations and recomputes the sample mean and variance until the mean converges to a fixed value with an error less than one decimal place. The likelihood threshold is then set at four standard deviations below the sample mean. This threshold corresponds to an average acceptance rate of 84.86 % for the MDRF calibration data of the modular cameras used in FastSPECT II. The acceptance rate can be adjusted by varying the likelihood threshold.

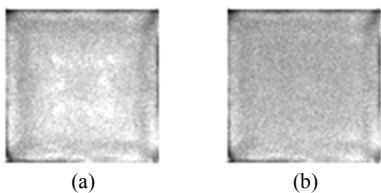


Fig. 7 Flood image of one modular camera in FastSPECT II. (a) Without likelihood windowing. (b) With position-dependent likelihood windowing.

Fig. 7 shows the flood image of one modular camera in FastSPECT II with and without likelihood windowing. The image was acquired with a point source placed at the center of the imager without the pinhole aperture cylinder in place. The cameras were in their mid-radial positions, which are 9.5 inches away from the imager axis. The point source was made of a single chromatographic resin bead 300 μm in diameter, and the source strength was 148 kBq. Each camera had 1000 cps on average while the background was about 70 cps/camera. The integration time was 35 minutes in order to acquire about 2-million events per camera. The flood images in Fig. 7 demonstrate the ability of likelihood window in scatter rejection and camera uniformity improvement.

D. Fourier Crosstalk Matrix and Spatial Resolution

The spatial resolution is a common indicator for the performance of an imaging system. It provides a measure of the shape and width of the point response function (PRF). Since tomographic systems are shift-variant, the PRF is a function of position in the FOV, and so is the spatial resolution. Therefore, it is useful to obtain a summary measure of the system resolution averaged over the FOV for comparing different systems. A measure of the system resolution based on the Fourier crosstalk matrix has been developed in [35]-[38]. This approach has been applied to other tomographic systems [38], [39] developed at CGRI to provide a summary measure of the spatial resolution for the hardware without considering any reconstruction algorithms.

The empirical computation of the Fourier crosstalk matrix by DFT of the measured \mathbf{H} -matrix elements is briefly introduced in this section. Details of the mathematical development can be found in [37] and [38]. Consider the FOV of the imager is confined to a cube of width L and an associated \mathbf{H} matrix with $N \times N \times N$ voxels. Hence the sampling interval $\Delta_L = L/N$. Denote the position vector $\mathbf{r}_n = \mathbf{n} \Delta_L$ for each voxel, where the index $\mathbf{n} = (n_x, n_y, n_z)$ and each component n_j takes integer values from 0 to $N-1$. Define the wavevector $\boldsymbol{\rho}_k = \mathbf{k}/L$ to represent a particular spatial frequency, where the index $\mathbf{k} = (k_x, k_y, k_z)$ and each component k_j takes integer values from 0 to $N-1$. Each diagonal element of the Fourier crosstalk matrix is the squared norm of the data when the object has a single spatial frequency, which can be approximated by the DFT of the \mathbf{H} -matrix elements [37]:

$$\beta_{\mathbf{k}\mathbf{k}} \propto \left| \sum_{\mathbf{m}} \sum_{n_x=0}^{N-1} \sum_{n_y=0}^{N-1} \sum_{n_z=0}^{N-1} H_{\mathbf{m}}(\mathbf{r}_n) \exp(-i2\pi \boldsymbol{\rho}_k \cdot \mathbf{r}_n) \right|^2. \quad (13)$$

Therefore $\beta_{\mathbf{k}\mathbf{k}}$ can be regarded as a generalized transfer function that specifies how strongly a particular frequency is transferred through the imaging system to the data. It has been shown that $\beta_{\mathbf{k}\mathbf{k}}$ is proportional to the square of the modulation transfer function (MTF^2) for a linear shift-invariant system [36]. More generally, $\beta_{\mathbf{k}\mathbf{k}}$ provides a mathematical measure to discuss the MTF of shift-variant imaging systems. It characterizes the response of a tomographic system through the projection-backprojection operator without involving any image reconstruction algorithms.

It is observed that $\beta_{\mathbf{k}\mathbf{k}}$ falls off roughly as the reciprocal of the spatial frequency [35]. This is the well-known fact in tomography that projection-backprojection operation without filtering results in much denser sampling in the low-frequency domain and leads to a strong low-pass filtering effect. A ramp-like filter is required to compensate this $1/|\boldsymbol{\rho}_k|$ fall-off. Therefore, an equivalent MTF^2 [38] is defined as

$$MTF_{eq}^2 = |\boldsymbol{\rho}_k| \frac{\beta_{\mathbf{k}\mathbf{k}}}{\beta_{00}}, \quad (14)$$

Assuming the MTF_{eq} along each axis (ρ_{kx} , ρ_{ky} , or ρ_{kz}) has an approximately Gaussian shape, its Fourier transform back in the space domain will also have a Gaussian form. The spatial resolution of the system is then defined as the FWHM of the Fourier transform of the MTF_{eq} along three axes. The spatial resolution along the j axis is given by

$$\begin{aligned} \text{Spatial resolution} &= FWHM \left(\mathfrak{F} \{ MTF_{eq}(\rho_j) \} \right) \\ &= \frac{4 \ln 2}{\pi} \frac{1}{FWHM(MTF_{eq}(\rho_j))}. \end{aligned} \quad (15)$$

This number cannot be interpreted as the width of the point

spread function (PSF) of the imaging system as it should be for a shift-invariant system. However, it can be regarded as the average spatial resolution over the FOV of an imager to provide a mathematical measure for comparing different imaging systems. Fig. 8 shows the normalized MTF_{eq}^2 along the three orthogonal axes of FastSPECT II. In each graph, the dots represent the values computed from a measured \mathbf{H} matrix on 1 mm grid and the line represents a best-fit Gaussian function to the data points. Since the value of MTF_{eq} at zero frequency is zero due to the ramp filter in (13), this data point is excluded in the curve fitting. Table 1 shows the spatial resolution of FastSPECT II computed from the Fourier crosstalk matrix along the three orthogonal axes by (15).

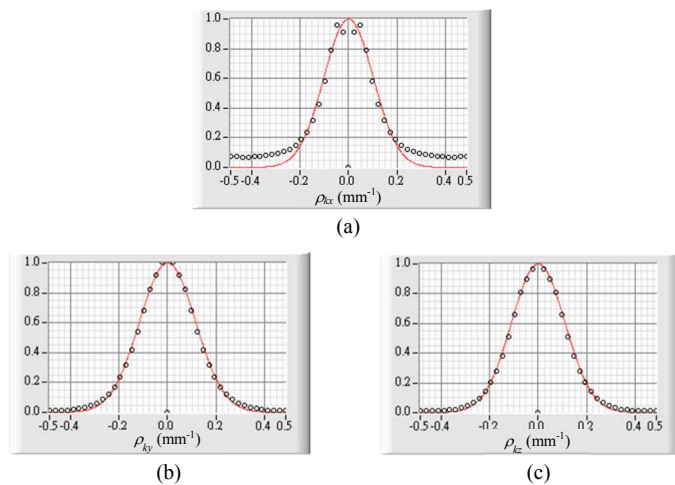


Fig. 8 Normalized MTF_{eq}^2 along three orthogonal axes of FastSPECT II. In each graph, the dots represent the values computed from the \mathbf{H} matrix and the line represents a best-fit Gaussian function. (a) Along the X axis. (b) Along the Y axis. (c) Along the Z axis.

TABLE I

SPATIAL RESOLUTION ESTIMATED BY THE FOURIER CROSSTALK	
Axis	Spatial Resolution (mm)
X (transverse)	2.60
Y (sagittal)	2.28
Z (coronal)	2.40

E. Hot-Rod Phantom Imaging

A miniature hot-rod phantom is imaged by FastSPECT II to visualize the spatial resolution of the imaging system. Fig. 9(a) shows the geometry of the hot-rod phantom. This phantom is made of a plastic cylinder containing three sectors of holes of different sizes (1.0, 1.5, and 2.0 mm in diameter). The distance between adjacent holes in each sector is three times of their diameters. The bore length is 12 mm. The phantom was filled with about 2.13 mCi of ^{99m}Tc -pertechnetate aqueous solution. This study had about 1700 counts/second (cps) per camera while the background was around 60 cps/camera. The acquired listmode data contained about 2-million events per camera. Fig. 9(b) shows the tomographic reconstructions of the phantom by using the Gaussian interpolated \mathbf{H} matrix on a 0.5 mm grid and

25 iterations of OS-EM with 4 subsets. The system is able to resolve the smallest rods in the phantom, which are 1 mm rods with 3 mm center-to-center distance. This is consistent with the spatial resolution estimated by the Fourier crosstalk matrix.

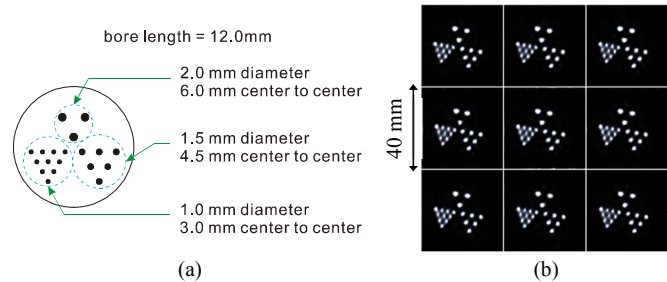


Fig. 9 Hot-rod phantom imaging. (a) Phantom geometry. (b) Tomographic reconstructions with 25 iterations of OS-EM with 4 subsets. The separation between slices is 0.5 mm.

IV. SMALL-ANIMAL IMAGING

Imaging studies of various mouse organs and tumors with different technetium-99m-labeled radiopharmaceuticals were performed to evaluate the performance of FastSPECT II. All tomographic images shown in this section were reconstructed with 25 iterations of OS-EM with 4 subsets. Images in sections IV-A to IV-C were reconstructed with 0.5 mm voxels, while the high-magnification images in section IV-D were reconstructed with 0.1 mm voxels.

A. Mouse Bone Scan

Bone scanning is a major clinical application of SPECT imaging in finding bone abnormalities, such as bone tumors, bone infections, and arthritis. It is also a common benchmark for evaluating the performance of a small-animal SPECT system. A 30-g mouse was tail-vein injected with 7 mCi of ^{99m}Tc -MDP in about 0.2 ml and imaged 3 hours after injection. The mouse was euthanized with a lethal dose of barbiturate via intra-peritoneal injection prior to imaging. As the body length was longer than the axial FOV of the imager, the mouse was imaged in six longitudinal positions with 20-mm movement in between. The integration time for the first animal position was 20 minutes and prolonged for subsequent animal positions to compensate for the radioactive decay. About 150,000 counts per animal position per camera were recorded.

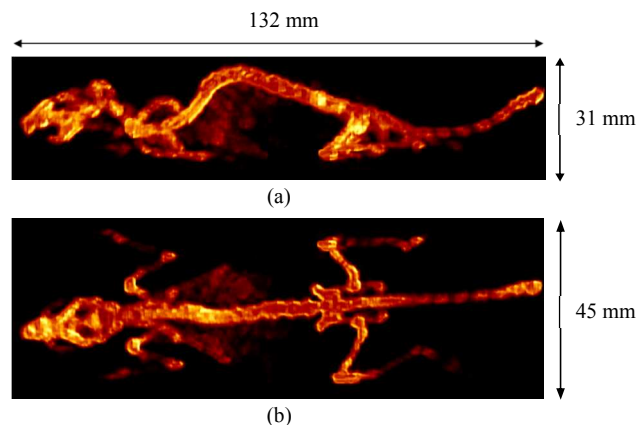


Fig. 10 Volume rendering of the mouse-bone scan: (a) side view; (b) top view.

Fig. 10 shows the volume rendering of the mouse skeleton. Major features of the skeleton are recognizable, such as the skull, the zygomatic bones, the mandibles, the scapulae, the vertebral column, the sterna, the ilia, and the front and hind limbs. Individual caudal vertebrate are clearly delineated. Anatomic details shown in these images illustrate the capability of FastSPECT II for high-resolution imaging.

B. Mouse Kidney Imaging

As many radiopharmaceuticals injected into the body are excreted through kidneys into urine, high radioactivity is typically shown in kidneys. Hence kidney imaging can serve as a performance yardstick of a SPECT system.

A mouse was injected with 5.96 mCi of ^{99m}Tc -Glucurate via the tail vein and imaged 45 minutes post-injection. Images were acquired for 10 minutes with about 15-million events recorded. Fig. 11 shows the tomographic reconstruction of the mouse kidneys. Nice uniform uptake is presented in the renal cortex.

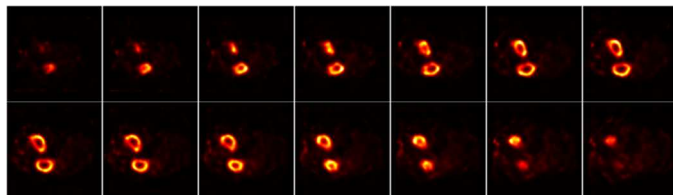


Fig. 11 Consecutive coronal slices of the mouse-kidney reconstruction with 0.5-mm separation between slices. The dimensions of each slice are 40 mm \times 40 mm.

C. Dynamic Mouse Imaging of Xenografted Human MDA-MB-231 Breast Cancer

The listmode data-acquisition electronics of FastSPECT II records the occurrence time of each event to a 30-nanosecond precision. The motionless characteristic of the imaging system along with the listmode data acquisition makes the data dynamic in nature. Therefore images can be reconstructed with any desired time slices. The integration time T controls the number of counts in each image and hence influences the noise statistics of the reconstructed image. The time difference ΔT between images can be adjusted to study the temporal variation of the tracer distribution. By imaging the flow and metabolism of the radiotracer, the dynamic imaging capability of FastSPECT II provides a valuable tool in studying the kinetic of pharmaceuticals. Potential applications include imaging myocardial and cerebral perfusion, targeting cell receptors, and assessing renal function.

A mouse model with xenografted human MDA-MB-231 breast cancer was imaged to investigate the dynamic imaging capability of FastSPECT II using a ^{99m}Tc -labeled integrin $\alpha_v\beta_3$ -specific cyclic (Arg-Gly-Asp) RGD peptide dimer, ^{99m}Tc -3P-RGD₂. Integrin $\alpha_v\beta_3$ is a receptor for a variety of extracellular matrix proteins with the exposed RGD tripeptide sequences and a key player in angiogenesis. ^{99m}Tc -3P-RGD₂ is very promising for imaging tumor angiogenesis because of enhanced integrin $\alpha_v\beta_3$ binding affinity for simultaneous dual receptor binding and rapid clearance kinetics from the normal organs, such as blood, liver and lungs [40].

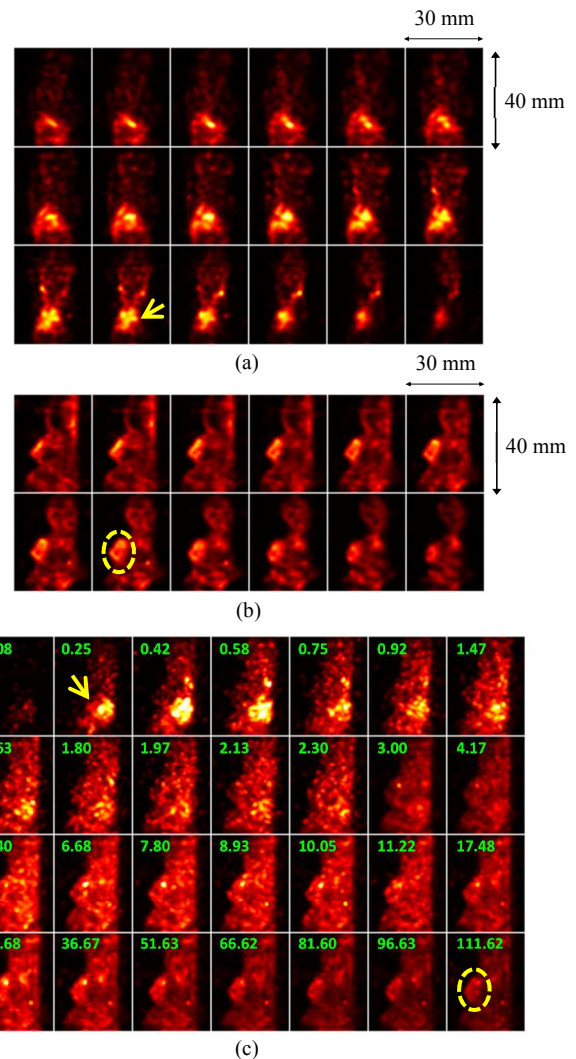


Fig. 12 Dynamic mouse imaging of xenografted human MDA-MB-231 breast cancer. Images are corrected for the integration time and radioactive decay. The cardiac blood pool is indicated by arrows and the tumor is indicated by dashed ellipses.

(a) Consecutive coronal slices showing the cardiac blood pool with 0.5 mm slice thickness. Images are reconstructed from the first 60 second integration.

(b) Consecutive sagittal slices from 10 minute integration at 120 minutes post injection, showing the tumor site with 0.5 mm slice thickness.

(c) Time sequence showing the maximum intensity re-projections of sagittal slices. The numbers in each subplot are the time post injection in minutes. The display scales in the first two rows are the same; the display scale of the third row is half of the first row, and the display scale of the fourth row is one-third of the first row.

The image acquisition began at the instant the radiotracer was intravenously injected via a tail vein catheter. The acquisition time was 1 minute for the first 10 image sessions. After that, 2-minute integration was acquired at 15 minutes post injection. Then, 7 image sessions were collected for 5-minute integration at 20, 30, 45, 60, 75, 90, and 105 minutes post injection. Finally, 10 minute integration was acquired at 120 minutes post injection.

Fig. 12 shows the tomographic reconstruction of the dynamic imaging study. In order to observe the uptake right after the injection, the images in the first 2 sessions (roughly the first 2.5 minutes) are additionally processed in 10-second steps with 10-second exposure ($T = \Delta T = 10$ sec). Images in Fig. 12(a)

are reconstructed from the data of the first 60 second integration, showing consecutive coronal slices of the cardiac blood pool with 0.5 mm slice thickness. Fig. 12(b) shows consecutive sagittal slices of the tumor site with 0.5 mm slice thickness, reconstructed from the data with 10 minute integration at 120 minutes post injection. Fig. 12(c) shows the time sequence of maximum intensity re-projections of sagittal slices so that the cardiac blood pool and tumor are visible in the same frame. The numbers in each subplot are the mid-point time post injection in each image reported in minutes. The images are corrected for the integration time and ^{99m}Tc decay.

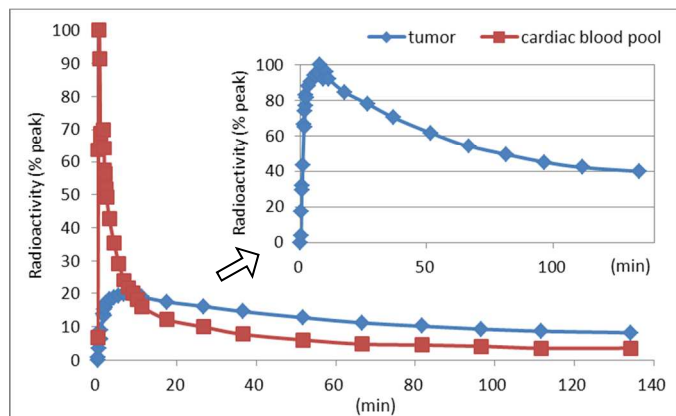


Fig. 13 Time-activity curves for the tumor site and the cardiac blood pool in the dynamic mouse imaging. The curves are normalized by the peak radioactivity in the cardiac blood pool. The inset is the time-activity curve of the tumor normalized by the peak uptake in the tumor.

Fig. 13 shows the time-activity curves (TACs) for the tumor site and the cardiac blood pool from 0 to 134.2 minutes post injection. Two elliptical regions of interest (ROIs), one enclosing the tumor volume and the other enclosing the cardiac blood pool, were created to determine the radioactive counts. Note that the time of the image session at 120 minutes post injection is corrected to 134.2 minutes; the time difference is between the lab notes and the actual computer time. The time of other image sessions is also corrected. The curves are normalized by the peak radioactivity in the blood pool. It can be observed that the radioactivity in the blood pool peaks at about 0.4 minutes post injection. The activity rapidly washes out to 50% around 2 minutes post injection and then keeps reducing to 10% at 26.7 minutes. The inset in Fig. 13 shows the TAC of the tumor normalized by the peak uptake in the tumor. The uptake and washout in the tumor shows a much slower rate than that of the blood pool. The radioactivity in the tumor peaks at 7.8 minutes post injection. The activity gradually reduces to 40% at 134 minutes post injection. These TACs can provide the information for modeling tracer kinetics.

D. High-Magnification Mouse-Femur Imaging

A high-magnification aperture is implemented in FastSPECT II to achieve sub-millimeter resolution. This aperture comprises two pieces, including a small pinhole collimator and its supporting cylinder as shown in Fig. 14. The aperture has an array of 100- μm -diameter pinholes, one per camera. Cameras are retracted to their farthest radial positions

(31.75 cm from the imager axis). The resulting magnification is about 18. The FOV is about 5 mm in three directions.

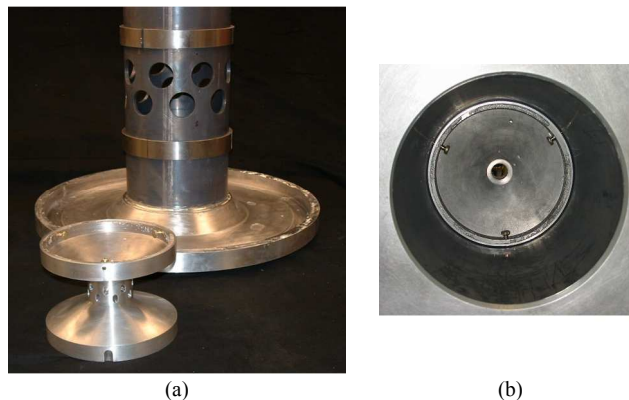


Fig. 14 High-magnification aperture of FastSPECT II. (a) The pinhole aperture (front) and its supporting cylinder (back). (b) The high-magnification aperture in place.

The radioactive point source used to calibrate this system was made of a single 200- μm -diameter chromatographic resin bead with an activity of 500 μCi . To compromise among the step size, the FOV, and the total acquisition time, the \mathbf{H} matrix was measured on a 400- μm grid with a scan size of $13 \times 13 \times 13$ points. The total acquisition time was about 10 hours. The \mathbf{H} matrix was then interpolated to a 100- μm grid for use in tomographic reconstruction, yielding a reconstruction voxel with a volume of 1 nL. The system sensitivity is about 607 cps/MBq with 16 cameras, and the background radiation is about 35 cps/camera.

In vivo mouse models of the metastatic bone lesions with neuroblastoma are useful for investigating disease progression and evaluating the response to therapy. SPECT imaging with the $18\times$ system provides high-resolution images and permits noninvasive and longitudinal studies. These strategies are also applicable to a variety of bone-tumor models, such as prostate and breast carcinoma.

A mouse model with neuroblastoma was prepared and imaged in collaboration with Rex Moats of the University of Southern California and Bret Abbott of the University of Arizona. One million human neuroblastoma cells were injected into the medullary space of the right femur three months before imaging. The mouse was injected with 9.5 mCi of ^{99m}Tc -MDP and imaged with the $18\times$ system 7 hours post injection. The affected femur was positioned in the FOV. SPECT images were acquired for 5 animal-bed positions, 5-minute integration per bed position. The movement between beds was 2 mm along the imager axis. About 1.4 million events were acquired and passed through the likelihood window of the ML position estimator. Tomographic reconstructions from different bed positions are stitched together based on the geometric movements and corrected for the radioactive decay. Fig. 15(a)-(c) show the tomographic slices of the mouse-femur and Fig. 15(d) shows the 3D volume rendering. The coronal slices shown in Fig. 15(b) demonstrate the neuroblastoma bone lesion and correlate with the X-ray CT image shown in Fig. 15(e). This study validates the capability of the $18\times$ system in investigating metastatic bone lesions.

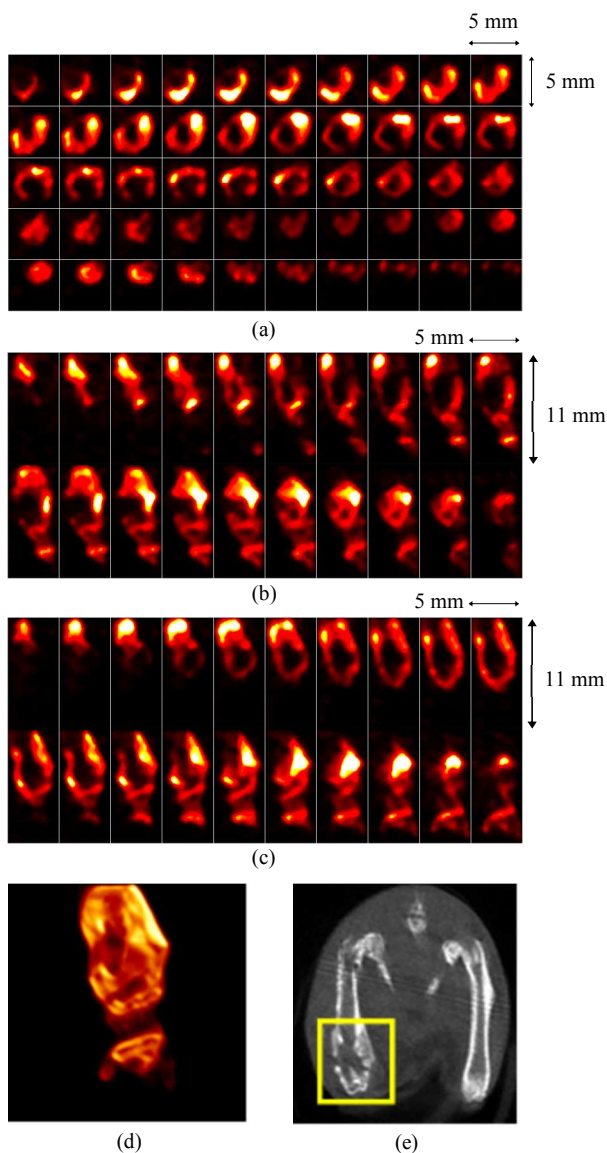


Fig. 15 Mouse-femur images.

- (a) Transverse slices, 0.2 mm separation between slices.
 (b) Coronal slices, 0.2 mm separation between slices.
 (c) Sagittal slices, 0.2 mm separation between slices.
 (d) Volume rendering of the SPECT reconstruction.
 (e) X-ray CT image of the mouse femur (Courtesy of Dr. M. Bret Abbott). The rectangle in the graph indicates the FOV of the SPECT images.

V. DISCUSSIONS

There are several areas of further development that can aid the performance of FastSPECT II, such as hardware modifications and data acquisition protocols. An integrated X-ray CT system called FaCT has been developed to make FastSPECT II a dual-modality instrument [41]. Co-registration of functional SPECT and anatomical CT images can have a favorable impact on the analysis of imaging studies. Moreover, as FastSPECT II has flexible aperture assemblies, it is possible to obtain higher sensitivity by employing multiple pinholes per camera. A table-top SPECT imager, the multi-module multi-resolution (M^3R) system [42], which utilizes four modular cameras and interchangeable pinhole plates, has been developed in this group. This system allows variation of system

magnification and multi-pinhole arrangement, and has been used for studying optimal system design for detection tasks. The centroid interpolation with Gaussian fitting method has been successfully implemented to interpolate the \mathbf{H} matrices of this multi-pinhole system.

Another beneficial hardware modification is to utilize the adaptive SPECT concept [43], [44]. An adaptive SPECT system can change its hardware configuration automatically based on the preliminary image data, in order to improve the image quality for a particular task. A small-animal adaptive SPECT system is currently under development at CGRI [45]. Each camera is mounted on a translation stage so that the object-to-camera distance can be adjusted continuously via real-time computer control. The aperture cylinder has several sections with different diameters to support various magnifications. The pinholes associated with each camera have computer controlled shutters to switch between single and multi-pinhole configurations.

The completeness condition of cone-beam tomography [46] requires that every plane intersecting the object support has to intersect the acquisition curve at least at one point. However, the sampling configuration of FastSPECT II, which comprises two parallel circular trajectories, does not satisfy the completeness condition. The planes containing each trajectory intersect the FOV right at the edges of the FOV. Therefore the shadow zone [46] in the Radon domain is located at the center of the FOV. Simulation studies of the Defrise phantom in Fig. 16 show artifacts in the reconstructed images, especially in the middle of the FOV. Adding translations along the imager axis into the data acquisition protocol nearly fulfills the completeness condition and reduces artifacts significantly, as shown in Fig. 16(c). Further investigations utilizing task-based assessment of image quality and aliasing analysis based on the Fourier crosstalk matrix are still required to determine the optimal translational image acquisitions.

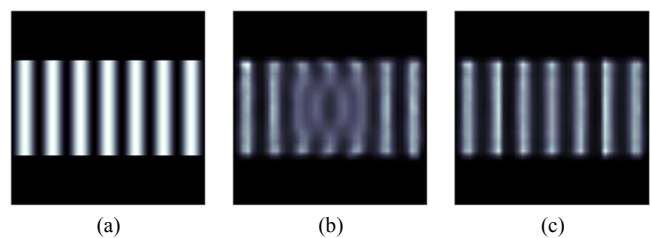


Fig. 16 Synthetic sinusoidal Defrise phantom along the imager axis.

- (a) Digital phantom, period = 5.75 mm.
 (b) Reconstruction without bed translation.
 (c) Reconstruction from 3 bed positions (translations at 0 and ± 10 mm).

VI. CONCLUSION

FastSPECT II is a stationary small-animal SPECT imager that allows selections of resolution and FOV for different imaging tasks. With the experimental calibration methods to take all of the system physics into account, FastSPECT II is now on-line for biomedical research. Imaging studies of various organs and tumors in mice have shown the dynamic imaging capability of the system and sub-millimeter resolution with the high-magnification configuration. Appropriate

hardware modifications to support multi-modality or adaptive imaging can make the instrument more comprehensive and better performance for specific tasks. The optimization of the data-acquisition protocol to fulfill the completeness condition of cone-beam tomography can consequently improve the image quality of the system. The utilization of higher resolution CCD-based gamma cameras as well as faster data processing hardware and software has brought the next generation FastSPECT III system.

ACKNOWLEDGMENT

The authors would like to thank Bret Abbott, Christy Barber, Cécile Chaix, Heather Durko, Noura Eleid, Lance Fesler, William Hunter, Robert Hunter, and Gail Stevenson for technical support, and Shuang Liu at Purdue University for providing us with ^{99m}Tc labeling kits of 3P-RGD₂ to image the mouse model with xenografted human MDA-MB-231 breast cancer. Special memories go to the late Donald Wilson, who contributed to the optical configuration design and image reconstruction algorithms.

REFERENCES

- [1] R. K. Rowe, J. N. Aarsvold, H. H. Barrett, J. C. Chen, W. P. Klein, B. A. Moore, I. W. Pang, D. D. Patton, and T. A. White, "A stationary hemispherical SPECT imager for three-dimensional brain imaging," *J. Nucl. Med.*, vol. 34, no. 3, pp. 474-480, 1993.
- [2] L. R. Furenlid, D. W. Wilson, Y. Chen, H. Kim, P. J. Pietraski, M. J. Crawford, and H. H. Barrett, "FastSPECT II: A second-generation high-resolution dynamic SPECT imager," *IEEE Trans. Nucl. Sci.*, vol. 51, no. 3, pp. 631-635, 2004.
- [3] F. J. Beekman, F. van der Have, B. Vastenhouw, A. J. A. van der Linden, P. P. van Rijk, J. P. H. Burbach, and M. P. Smidt, "U-SPECT-I: A novel system for submillimeter-resolution tomography with radiolabeled molecules in mice," *J. Nucl. Med.*, vol. 46, pp. 1194-1200, 2005.
- [4] T. Funk, P. Després, W. C. Barber, K. S. Shah, and B. H. Hasegawa, "A multipinhole small animal SPECT system with submillimeter spatial resolution," *Med. Phys.*, vol. 33, no. 5, pp. 1259-1268, 2006.
- [5] F. van der Have, B. Vastenhouw, R. M. Ramakers, W. Branderhorst, J. O. Kraaij, C. Ji, S. G. Staelens, and F. J. Beekman, "U-SPECT-II: an ultrahigh-resolution device for molecular small-animal imaging," *J. Nucl. Med.*, vol. 50, pp. 599-605, 2009.
- [6] B. W. Miller, L. R. Furenlid, S. K. Moore, H. B. Barber, V. V. Nagarkar, and H. H. Barrett, "System integration of FastSPECT III, a dedicated SPECT rodent-brain imager based on BazookaSPECT detector technology," in *IEEE Nucl. Sci. Symp. Conf. Rec.*, pp. 4004-4008, 2009.
- [7] W. P. Klein, H. H. Barrett, I. W. Pang, D. D. Patton, M. M. Rogulski, J. D. Sain, and W. E. Smith, "FASTSPECT: Electrical and mechanical design of a high-resolution dynamic SPECT imager," in *Proc. 1995 IEEE NSS/MIC Conf. Rec.*, vol. 2, pp. 931-933, 1995.
- [8] B. W. Miller, "High-resolution gamma-ray imaging with columnar scintillators and CCD/CMOS sensors, and FastSPECT III: A third-generation stationary SPECT imager," Ph.D. dissertation, College of Opt. Sci., University of Arizona, Tucson, AZ, 2011.
- [9] G. K. Kastis, H. B. Barber, H. H. Barrett, H. C. Gifford, I. W. Pang, D. D. Patton, J. D. Sain, G. Stevenson, and D. W. Wilson, "High resolution SPECT imager for three-dimensional imaging of small animals," *J. Nucl. Med.*, vol. 39, no. 5-suppl., p. 9P, 1998.
- [10] T. D. Milster, L. A. Selberg, H. H. Barrett, R. L. Easton, G. R. Rossi, J. Arendt, and R. G. Simpson, "A modular scintillation camera for use in nuclear medicine," *IEEE Trans. Nucl. Sci.*, vol. 31, pp. 575-580, 1984.
- [11] J. N. Aarsvold, H. H. Barrett, J. Chen, A. L. Landesman, T. D. Milster, D. D. Patton, T. J. Roney, R. K. Rowe, R. H. Seacat III and L. M. Strimbu, "Modular scintillation cameras: a progress report," *Proc. SPIE*, vol. 914, pp. 319-325, 1988.
- [12] T. D. Milster, J. N. Aarsvold, H. H. Barrett, A. L. Landesman, L. S. Mar, D. D. Patton, T. J. Roney, R. K. Rowe, and R. H. Seacat III, "A full-field modular gamma camera," *J. Nucl. Med.*, vol. 5, no. 31, pp. 632-639, 1990.
- [13] H. H. Barrett, T. White, and L. C. Parra, "List-mode likelihood," *J. Opt. Soc. Amer. A*, vol. 14, no. 11, pp. 2914-2923, 1997.
- [14] J. E. Koss, D. L. Kirch, E. P. Little, T. K. Johnson, and P. P. Steele, "Advantages of listmode acquisition of dynamic cardiac data," *IEEE Trans. Nucl. Sci.*, vol. 44, no. 6, pp. 2431-2438, 1997.
- [15] L. C. Parra and H. H. Barrett, "List-mode likelihood: EM algorithm and image quality estimation demonstrated on 2-D PET," *IEEE Trans. Med. Imaging*, vol. 17, pp. 228-235, 1998.
- [16] A. Lehovich, "List-mode SPECT reconstruction using empirical likelihood," Ph.D. dissertation, Dept. Appl. Math., University of Arizona, Tucson, AZ, 2005.
- [17] L. Caucci and H. H. Barrett, "Objective assessment of image quality. V. Photon-counting detectors and list-mode data," *J. Opt. Soc. Am. A*, vol. 29, no. 6, pp. 1003-1016, 2012.
- [18] L. R. Furenlid, J. Y. Hesterman, and H. H. Barrett, "Real-time data acquisition and maximum-likelihood estimation for gamma cameras," in *Proc. 2005 14th IEEE-NPSS Real Time Conf. Rec.*, No. P5-8, Stockholm, Sweden, June 4-10, 2005.
- [19] J. Y. Hesterman, L. Caucci, M. A. Kupinski, H. H. Barrett, and L. R. Furenlid, "Maximum-likelihood estimation with a contracting-grid search algorithm," *IEEE Trans. Nucl. Sci.*, vol. 57, no. 3, pp. 1077-1084, 2010.
- [20] Y. C. Chen, "System calibration and image reconstruction for a new small-animal SPECT system," Ph.D. dissertation, College of Opt. Sci., University of Arizona, Tucson, AZ, 2006.
- [21] W. C. J. Hunter, "Modeling stochastic processes in gamma-ray imaging detectors and evaluation of a multi-anode PMT scintillation camera for use with maximum-likelihood estimation methods," Ph.D. dissertation, Dept. Phys., University of Arizona, Tucson, AZ, 2007.
- [22] H. H. Barrett and K. J. Myers, *Foundations of Image Science*, pp. 1200-1206, Wiley-Interscience, Hoboken, NJ, 2004.
- [23] M. D. Tipton, "The ODCAT: one dimensional coded aperture tomography," *Proc. SPIE*, vol. 152, pp. 113-120, 1978.
- [24] D. Lefkopoulos, J. Fonroget, J. Y. Devaux, J. B. Guilhem, J. C. Roucaeyrol, and R. Guiraud, "Quantitative 3D imaging with coded apertures by using SVD decomposition of the transmission matrix," in *Nuclear Medicine and Biology Advances: Proceedings of the Third World Congress of Nuclear Medicine and Biology, August 29 to September 2, 1982, Paris, France*, C. Raynaud ed., pp. 503-506, Pergamon Press, Oxford, 1983.
- [25] T. J. Roney, "Coded-aperture transaxial tomography using modular gamma cameras," Ph.D. dissertation, Opt. Sci. Center, University of Arizona, Tucson, AZ, 1989.
- [26] R. K. Rowe, "A system for three-dimensional SPECT without motion," Ph.D. dissertation, Opt. Sci. Center, University of Arizona, Tucson, AZ, 1991.
- [27] Y. C. Chen, L. R. Furenlid, D. W. Wilson, and H. H. Barrett, "Calibration of scintillation cameras and pinhole SPECT imaging systems," in *Small-Animal SPECT Imaging*, M. A. Kupinski and H. H. Barrett eds., pp. 195-201, Springer, New York, NY, 2005.
- [28] H. H. Barrett and W. Swindell, *Radiological Imaging: The Theory of Image Formation, Detection, and Processing*, Academic Press, San Diego, CA, 1981.
- [29] S. Metzler, J. Bowsher, K. Greer, and R. Jaszczak, "Analytic determination of the pinhole collimator's point-spread function and RMS resolution with penetration," *IEEE Trans. Med. Imaging*, vol. 21, no. 8, pp. 878-887, 2002.
- [30] W. H. Press, S. A. Teukolsky, W. T. Vetterling, and B. P. Flannery, *Numerical Recipes in C: The Art of Scientific Computing*, 2nd ed., Cambridge University Press, Cambridge, 1992.
- [31] H. H. Barrett, "Detectors for small-animal SPECT II: Statistical limitations and estimation methods," in *Small-Animal SPECT Imaging*, M. A. Kupinski and H. H. Barrett eds., pp. 49-86, Springer, New York, NY, 2005.
- [32] H. H. Barrett, W. C. J. Hunter, B. W. Miller, S. K. Moore, Y. C. Chen, and L. R. Furenlid, "Maximum-likelihood methods for processing signals from gamma-ray detectors," *IEEE Trans. Nucl. Sci.*, vol. 56, no. 3, pp. 725-735, 2009.
- [33] J. C. Chen and H. H. Barrett, "Likelihood window, energy window, and Bayesian window for scatter rejection in gamma cameras," in *IEEE Nucl. Sci. Symp. Conf. Record*, pp. 1414-1416, 1993.
- [34] J. C. Chen, "Scatter rejection in gamma cameras for use in nuclear medicine," *Comput. Med. Imaging Graph.*, vol. 21, pp. 283-291, 1997.
- [35] H. H. Barrett and H. C. Gifford, "Cone-beam tomography with discrete data sets," *Phys. Med. Biol.*, vol. 39, no. 3, pp. 451-476, 1994.

- 1
2
3
4
5
6
7
8
9
10
11
12
13
14
15
16
17
18
19
20
21
22
23
24
25
26
27
28
29
30
31
32
33
34
35
36
37
38
39
40
41
42
43
44
45
46
47
48
49
50
51
52
53
54
55
56
57
58
59
60
- [36] H. H. Barrett, J. L. Denny, R. F. Wagner, and K. J. Myers, "Objective assessment of image quality. II. Fisher information, Fourier crosstalk, and figures of merit for task performance," *J. Opt. Soc. Am. A*, vol. 12, no. 5, pp. 834-852, 1995.
- [37] H. C. Gifford, "Theory and application of Fourier crosstalk: An evaluator for digital-system design," Ph.D. dissertation, Dept. Appl. Math., University of Arizona, Tucson, AZ, 1997.
- [38] H. Kim, L. R. Furenlid, M. J. Crawford, D. W. Wilson, H. B. Barber, T. E. Peterson, W. C. J. Hunter, Z. Liu, J. M. Woolfenden, and H. H. Barrett, "SemiSPECT: A small-animal single-photon emission computed tomography (SPECT) imager based on eight cadmium zinc telluride (CZT) detector arrays," *Med. Phys.*, vol. 33, no. 2, pp. 465-474, 2006.
- [39] G. K. Kastis, "Multi-modality imaging of small animals," Ph.D. dissertation, Opt. Sci. Center, University of Arizona, Tucson, AZ, 2002.
- [40] Z. Liu, B. Jia, J. Shi, X. Jin, H. Zhao, F. Li, S. Liu, and F. Wang, "Tumor uptake of the RGD dimeric probe (^{99m}Tc -G(3)-2P(4)-RGD2 is correlated with integrin $\alpha(v)\beta(3)$ expressed on both tumor cells and neovasculature," *Bioconj. Chem.*, vol. 21, no. 3, pp. 548-555, 2010.
- [41] J. W. Moore, "Adaptive X-ray computed tomography," Ph.D. dissertation, College of Opt. Sci., University of Arizona, Tucson, AZ, 2011.
- [42] J. Y. Hesterman, M. A. Kupinski, L. R. Furenlid, D. W. Wilson, and H. H. Barrett, "The multi-module, multi-resolution system (M3R): a novel small-animal SPECT system," *Med. Phys.*, vol. 34, no. 3, pp. 987-993, 2007.
- [43] M. Freed, M. A. Kupinski, L. R. Furenlid, D. W. Wilson, and H. H. Barrett, "A prototype instrument for single pinhole small animal adaptive SPECT imaging," *Med Phys.*, vol. 35, no. 5, pp. 1912-1925, 2008.
- [44] H. H. Barrett, L. R. Furenlid, M. Freed, J. Y. Hesterman, M. A. Kupinski, E. Clarkson, and M. K. Whitaker, "Adaptive SPECT," *IEEE Trans. Med. Imag.*, vol. 27, no. 6, pp. 775-788, 2008.
- [45] C. Chaix, J. W. Moore, R. Van Holen, H. H. Barrett, and L. R. Furenlid, "The adaptiSPECT Imaging Aperture," in *IEEE Nucl. Sci. Symp. and Med. Imaging Conf. Record*, pp. 3564-3567, 2012.
- [46] P. Grangeat, "Mathematical framework of cone-beam 3D reconstruction via the first derivative of the Radon transform," in *Mathematical Methods in Tomography* (Lecture Notes in Mathematics, vol. 1497), G T Herman, A. K. Louis and F. Natterer eds., pp. 66-97, Springer, Berlin, 1991.